RESEARCH PAPER

Local field potentials, spiking activity, and receptive fields in human visual cortex

Lu Luo[1,2†], Xiongfei Wang[3,4†], Junshi Lu[1,5], Guanpeng Chen[1,5,6], Guoming Luan[3,4,7], Wu Li[8], Qian Wang[1,5*] & Fang Fang[1,5,6*]

[1]School of Psychological and Cognitive Sciences and Beijing Key Laboratory of Behavior and Mental Health, Peking University, Beijing 100871, China;
[2]School of Psychology, Beijing Sport University, Beijing 100084, China;
[3]Department of Neurosurgery, Sanbo Brain Hospital, Capital Medical University, Beijing 100093, China;
[4]Beijing Key Laboratory of Epilepsy, Epilepsy Center, Sanbo Brain Hospital, Capital Medical University, Beijing 100093, China;
[5]IDG/McGovern Institute for Brain Research, Peking University, Beijing 100871, China;
[6]Peking-Tsinghua Center for Life Sciences, Peking University, Beijing 100871, China;
[7]Beijing Institute for Brain Disorders, Beijing 100069, China;
[8]State Key Laboratory of Cognitive Neuroscience and Learning and IDG/McGovern Institute for Brain Research, Beijing Normal University, Beijing 100875, China

†Contributed equally to this work
*Corresponding authors (email: Fang Fang, email: ffang@pku.edu.cn; Qian Wang, email: wangqianpsy@pku.edu.cn)

The concept of receptive field (RF) is central to sensory neuroscience. Neuronal RF properties have been substantially studied in animals, while those in humans remain nearly unexplored. Here, we measured neuronal RFs with intracranial local field potentials (LFPs) and spiking activity in human visual cortex (V1/V2/V3). We recorded LFPs via macro-contacts and discovered that RF sizes estimated from low-frequency activity (LFA, 0.5–30 Hz) were larger than those estimated from low-gamma activity (LGA, 30–60 Hz) and high-gamma activity (HGA, 60–150 Hz). We then took a rare opportunity to record LFPs and spiking activity via microwires in V1 simultaneously. We found that RF sizes and temporal profiles measured from LGA and HGA closely matched those from spiking activity. In sum, this study reveals that spiking activity of neurons in human visual cortex could be well approximated by LGA and HGA in RF estimation and temporal profile measurement, implying the pivotal functions of LGA and HGA in early visual information processing.

human visual cortex | receptive field | intracranial EEG | local field potential | spiking activity

INTRODUCTION

Neurons in visual cortex initially encode the external world in a fragmental manner by restrictively responding to stimuli in a small portion of the visual field, namely the receptive field (RF) (Hubel and Wiesel, 1959). For decades, the RF concept, which interprets how external information is processed and represented internally, has served as a Rosetta stone of neuroscience. RF properties, such as size and location, are typically measured based on single-neuron activity. Since it is extremely rare to record single-neuron activity in humans due to technical difficulties and ethical considerations (Mamelak, 2014), our understanding of neuronal RF properties mainly derives from animal studies (Andoni et al., 2013). RFs in human visual cortex have been predominantly explored in functional magnetic resonance imaging (fMRI) studies using the population receptive field (pRF) method, which indirectly measures the collective RF of all active neurons in a voxel based on blood-oxygenation-level-dependent (BOLD) signals (Dumoulin and Wandell, 2008; Wandell et al., 2007; Wandell and Winawer, 2015), leaving the neuronal RF properties in humans nearly unknown. This long-overlooked barrier raises an intractable question: can neuronal RF properties in animals, even in non-human primates, be used to explain human visual perception (Werner and Spillmann, 1990)? Given accumulating evidence

demonstrating anatomical and functional differences between human and non-human primate brains (Beaulieu-Laroche et al., 2018; Boldog et al., 2018; Kaas and Herculano-Houzel, 2017; Pryluk et al., 2019), it now becomes urgent to explore RF properties in human subjects through direct measurement of neuronal activities, such as local field potentials (LFPs) and spiking activity.

In vivo extracellular recording studies in human visual cortex are extremely rare. Using microwire recording in neurosurgery patients, two pioneering studies tried to map visual RFs based on spiking activity (Marg et al., 1968; Wilson et al., 1983). However, the precise locations of microwires were unclear due to technological limitations at that time. To the best of our knowledge, the only quantitative description of neuronal RFs estimated from multi-unit activities was obtained via two microwires implanted in V2/V3, which suggests that the RF sizes in humans were comparable to those in macaques (Self et al., 2016).

Most intracranial studies exploring RF properties in human visual cortex are based on LFPs recorded via macro-contacts (Bosking et al., 2017; Self et al., 2016; Winawer et al., 2013; Winawer and Parvizi, 2016; Yoshor et al., 2007). LFP components are generated by neural circuits at various spatial scales and can be functionally heterogeneous in visual processing (Bartoli et al., 2019; Han et al., 2021; Hermes et al., 2014; van

Kerkoerle et al., 2014). Therefore, RFs estimated from different LFP components could differ in size and location. For example, Winawer and colleagues (Winawer et al., 2013) found that RFs estimated from asynchronous and stimulus-locked LFP components slightly differed in size and location.

A fundamental question in neurophysiology is the relationship between LFPs and spiking activity. More specifically, can LFPs approximate spiking activity in RF estimation? This issue has been extensively investigated in animal studies (Belitski et al., 2008; Burns et al., 2010; Klink et al., 2021; Rasch et al., 2008; Ray et al., 2008a; Ray and Maunsell, 2011a; Ray and Maunsell, 2011b). In humans, the relationship between LFP components and spiking activity has been examined in auditory cortex (Mukamel et al., 2005; Mukamel et al., 2011; Nir et al., 2007; Zanos et al., 2012), motor cortex (Perge et al., 2014), and prefrontal cortex (Leszczyński et al., 2020). While some studies revealed a robust temporal correlation between spiking activity and high-frequency LFP components (Mukamel et al., 2005; Mukamel et al., 2011; Perge et al., 2014), others did not (Leszczyński et al., 2020; Nir et al., 2007; Zanos et al., 2012). Notably, this issue has never been examined in human visual cortex.

In the current study, we applied RF mapping procedures and intracranially recorded LFPs and spiking activity in human visual cortex (V1/V2/V3) to (i) quantify and compare neuronal RF properties estimated from different types of signals and (ii) examine the temporal relationships between these signals. We first recorded LFPs via macro-contacts in 22 subjects undergoing invasive monitoring for the purpose of treating drug-resistant epilepsy (Experiments 1 and 2) (Figure S1 and Table S1 in Supporting Information). Then, in 2 of the 22 subjects, we simultaneously recorded LFPs and spiking activity via microwires (Experiment 3) (Table S2 in Supporting Information). Based on a V1-V3 atlas (Benson et al., 2014) applied to the pre-implant T1-weighted MRI scan of individual subjects, we identified 244 macro-contacts localized in V1-V3 and 18 microwires in V1 (Figure S1 and Table S1 in Supporting Information). LFPs were separated into three components: low-frequency activity (LFA, 0.5–30 Hz), low-gamma activity (LGA, 30–60 Hz), and high-gamma activity (HGA, 60–150 Hz) (Bartoli et al., 2019; Parvizi and Kastner, 2018).

RESULTS

RFs estimated from LFA, LGA, and HGA

Experiment 1 aimed to compare locations and sizes of RFs estimated from LFA, LGA, and HGA. All subjects underwent a preliminary RF mapping procedure with 3°×3° checkerboard stimuli (Figure 1A). To maintain fixation at the center of the screen, subjects were required to respond to color changes of the central fixation point throughout the experiment (response accuracy: 95.2%±0.9%, mean±SEM). Meanwhile, a 3°×3° checkerboard was briefly presented at one of 99 (11×9 grid covering the full visual field) or 54 (6×9 grid covering the contralateral visual field) mapping positions (Yoshor et al., 2007).

We identified visually responsive macro-contacts by the presence of broadband visually evoked LFPs (0.5–200 Hz) to at least one mapping position (Figure 1C). Of all 244 macro-contacts in visual cortex, 219 (89.8 %) were visually responsive (V1: $n_{contact}$=110; V2: $n_{contact}$=66; V3: $n_{contact}$=43). Next, we filtered the broadband LFPs into LFA, LGA, and HGA. 98.6% (216/219), 72.1% (158/219), and 74.4% (163/219) macro-contacts exhibited significant visually evoked LFA, LGA, and HGA, respectively (Figure 1C and D; Table S1 in Supporting Information).

For each visually responsive macro-contact, we estimated RFs from LFA, LGA, and HGA (i.e., RF_{LFA}, RF_{LGA}, and RF_{HGA}) separately, adopting a two-dimensional (2D)-Gaussian fitting method described in previous ECoG studies (Nir et al., 2007; Yoshor et al., 2007). The size and location of an RF were defined as the averaged full width at half maximum (FWHM) of the two axes and the center of the fitted Gaussian function, respectively. RFs centered at or outside the border of the grids were excluded from further analyses. In total, we identified RF_{LFA}, RF_{LGA}, and RF_{HGA} for 81 macro-contacts (V1: $n_{contact}$=41; V2: $n_{contact}$=29; V3: $n_{contact}$=11).

Figure 2A shows the estimations of RF_{LFA}, RF_{LGA}, and RF_{HGA} in an example V1 macro-contact (P440, macro-contact V01). We observed that the three RFs differed: the sizes of RF_{LGA} (size=2.1°, location=[2.6°, −7.3°; azimuth, elevation]) and RF_{HGA} (size=2.2°, location=[2.6°, −6.3°]) were smaller than that of RF_{LFA} (size=3.7°, location=[1.3°, −5.6°]). A one-way repeated-measures ANOVA found a significant main effect of LFP component (LFA/LGA/HGA; $F_{2,160}$=22.042, P=3.506×10^{-9}). Post hoc tests showed that the mean sizes of RF_{LGA} (2.2°±0.1°) and RF_{HGA} (2.4°±0.2°) were significantly smaller than that of RF_{LFA} (3.3°±0.2°; RF_{LFA} vs. RF_{LGA}: P=1.289×10^{-6}; RF_{LFA} vs. RF_{HGA}: P=2.179×10^{-6}, Bonferroni corrected; Figure 2B and C). No significant size difference was found between RF_{LGA} and RF_{HGA} (P=0.641). The RF sizes estimated from LFPs were within the range of previous estimations from LFPs in human subjects (Self et al., 2016; Yoshor et al., 2007). We then compared the locations of RF_{LFA}, RF_{LGA}, and RF_{HGA} in the polar coordinate system. One-way repeated-measures ANOVAs showed that there was no significant difference in either eccentricity ($F_{2,160}$=1.896, P=0.153) or polar angle ($F_{2,160}$=0.954, P=0.387).

Although the 3°×3° checkerboard stimuli used in Experiment 1 enabled us to identify RF locations quickly, their relatively large size inevitably led to an overestimation of RF sizes. Therefore, in Experiment 2, we performed a second mapping procedure with five subjects ($n_{contact}$=17) using 1°×1° checkerboard stimuli (i.e., 1°×1° RF mapping; Figure 1B). We found that RF sizes estimated using 3°×3° checkerboard stimuli (RF_{LFA}: 2.6°±0.3°; RF_{LGA}: 1.8°±0.1°; RF_{HGA}: 2.2°±0.26°) were systematically larger than those estimated using 1°×1° checkerboard stimuli (RF_{LFA}: 1.4° ±0.2°; RF_{LGA}: 0.9°±0.2°; RF_{HGA}: 1.1°±0.2°; Figure 2D and E). A two-way repeated-measures ANOVA of Stimulus size (3°×3°/1°×1°)×LFP component (LFA/LGA/HGA) showed that both main effects were significant (Stimulus size: $F_{1,16}$=54.438, P=1.558×10^{-6}; LFP component: $F_{2,32}$=6.483, P=0.004; Figure 2F). No significant interaction effect was found ($F_{2,32}$=0.415, P=0.664). The sizes of RF_{LGA} and RF_{HGA} were still significantly smaller than those of RF_{LFA} (RF_{LFA} vs. RF_{LGA}: P=0.046; RF_{LFA} vs. RF_{HGA}: P=0.031; post hoc tests), while no significant difference was found between RF_{LGA} and RF_{HGA} (P=0.223; Figure 2F), consistent with the findings in Experiment 1. We then compared RF locations using two-way repeated-measures ANOVAs (Stimulus size×LFP component). No significant main effect and interaction were found in either eccentricity (Stimulus size: $F_{1,16}$=0.097, P=0.759; LFP component: $F_{2,32}$=0.330, P=0.721;
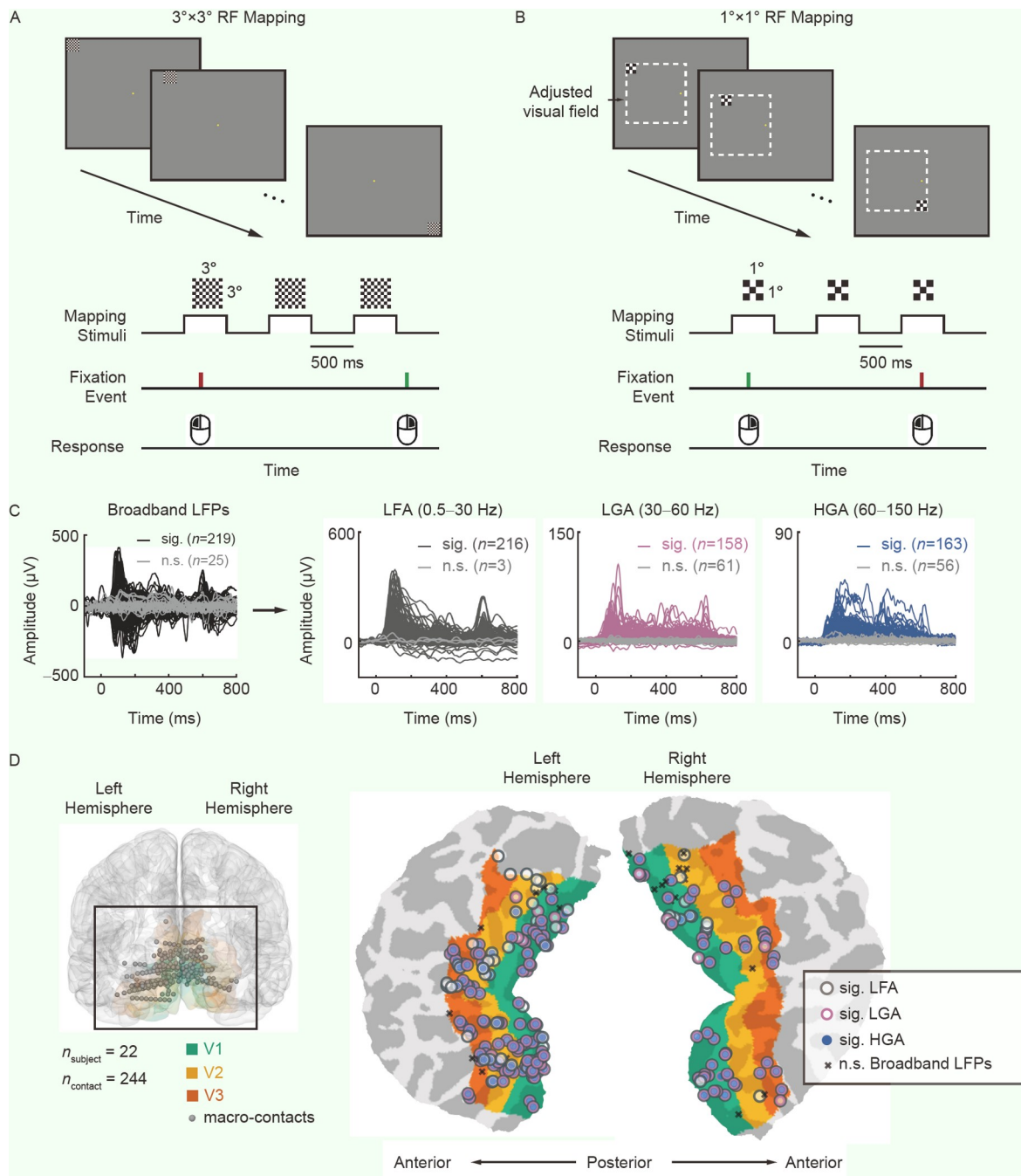
Figure 1. RF mapping procedures, visually evoked responses, and macro-contact locations. A, Schematic description of the 3°×3° RF mapping procedure used in Experiment 1. Subjects performed a fixation task while a 3°×3° checkerboard stimulus was flashed at different positions on the monitor. B, Schematic description of the 1°×1° RF mapping procedure used in Experiments 2 and 3. Subjects performed a fixation task while a 1°×1° checkerboard stimulus was flashed at different positions within an adjusted visual field (dashed box), which covered the responsive visual field in Experiment 1. C, Visually evoked responses recorded from macro-contacts in Experiment 1. Waveforms of significant broadband LFPs (black), LFA (dark grey), LGA (pink), and HGA (blue) and non-significant waveforms (light grey) are shown. D, Locations of macro-contacts visualized on a 3-dimensional template brain (left) and a flattened occipital patch (right; see Figure S1 in Supporting Information for locations of macro-contacts in individual brains). The colors on the brain indicate the retinotopic areas of interest (green: V1; orange: V2; red: V3). On the flattened occipital patch, the symbols indicate the significant LFP components identified for each macro-contact (grey annulus: LFA; pink annulus: LGA; blue circle: HGA). Macro-contacts without significant broadband LFPs were marked with black crosses. Sig., significant; n.s., not significant.

interaction: $F_{2,32}=1.153$, $P=0.328$) or polar angle (Stimulus size: $F_{1,16}=1.249$, $P=0.280$; LFP component: $F_{2,32}=1.222$, $P=0.307$; interaction: $F_{2,32}=0.021$, $P=0.979$). Together, these results demonstrate that the sizes of RF_{LFA} are remarkably larger than those of RF_{LGA} and RF_{HGA}, while the locations of these three RFs are nearly identical.

We considered two possible explanations for the larger size of RF_{LFA}. First, LFA may be modulated by feedback projections from neurons in higher visual cortex (Bastos et al., 2015; Jensen et al., 2015; Michalareas et al., 2016; van Kerkoerle et al., 2014), which have large RF sizes (Dumoulin and Wandell, 2008). If so, the latency of LFA should be longer than those of LGA and HGA.
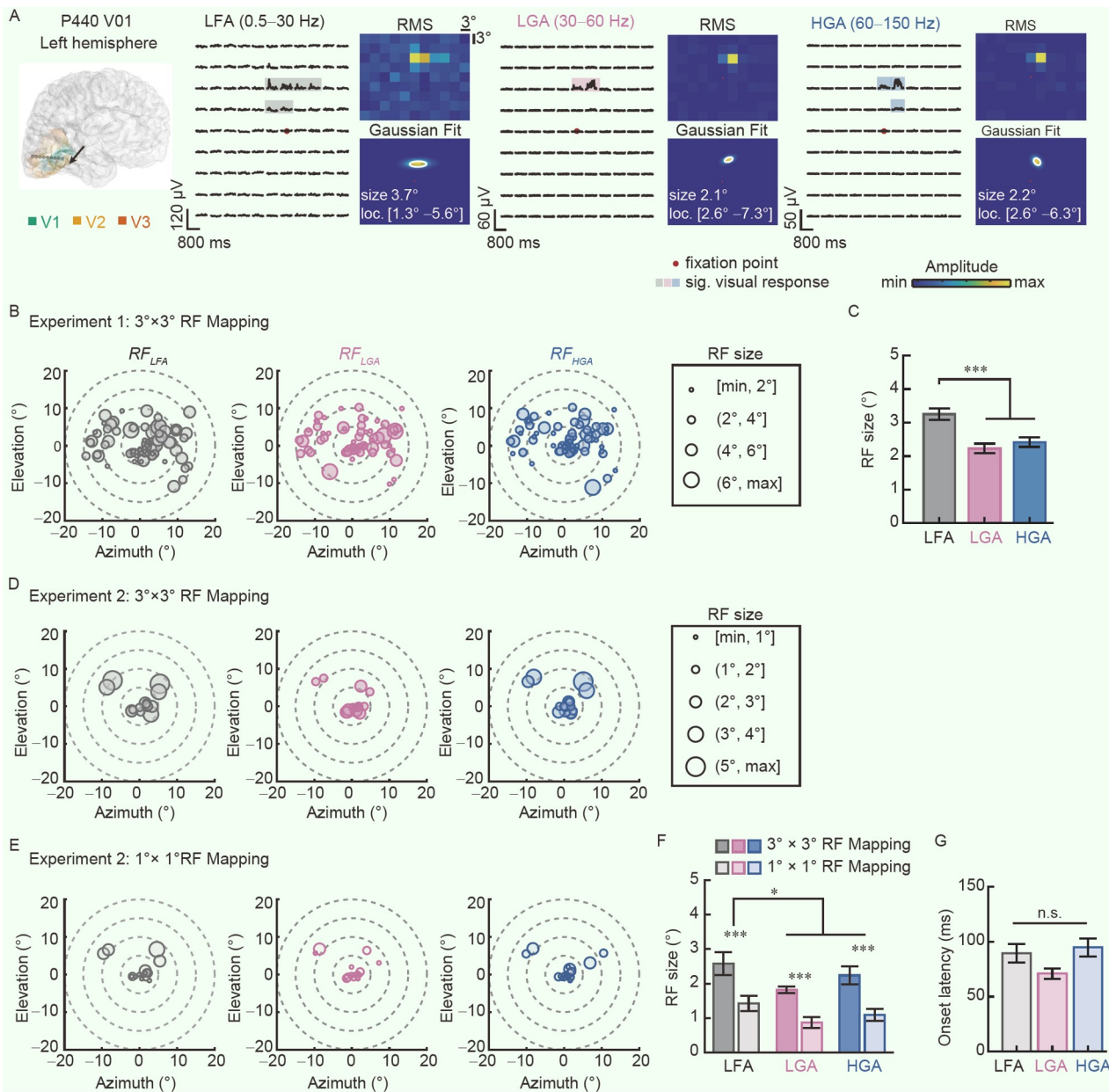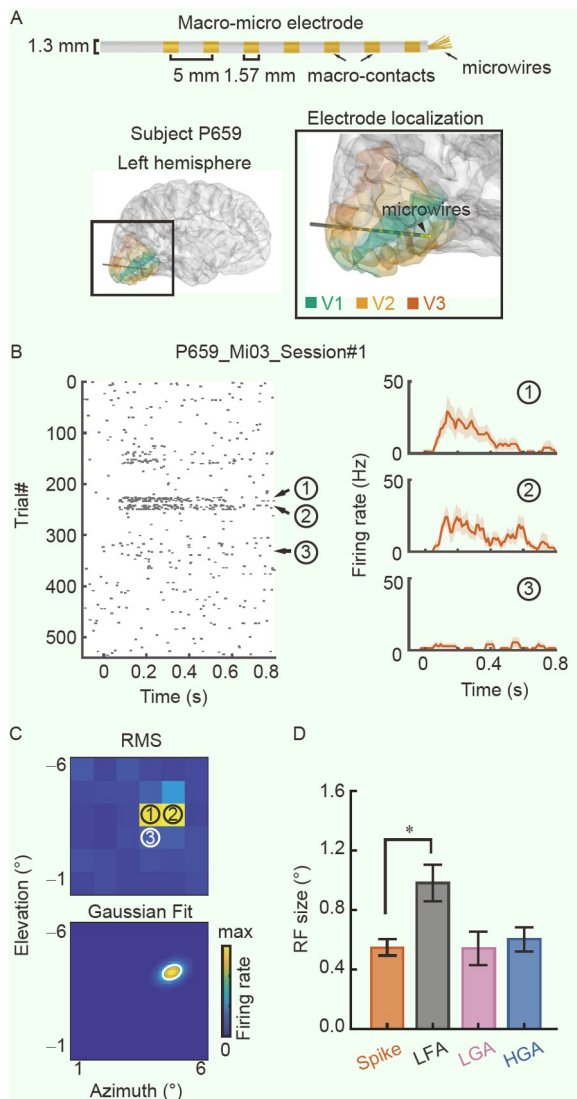
Figure 2. RF_LFA, RF_LGA, and RF_HGA mapping using macro-contacts. A, Locations and sizes of the RF_LFA, RF_LGA, and RF_HGA estimated in an example macro-contact (subject P440, macro-contact V01). The stereo-electrode with macro-contacts is visualized in P440's brain. For each LFP component, the averaged response waveforms to mapping positions (red dot: fixation point; translucent areas: significant responses), the RMS map, and the 2D Gaussian fit of the RMS map are shown. The white ellipses show the RF contours. B, Locations and sizes of RF_LFA, RF_LGA, and RF_HGA estimated with 3°×3° checkerboard stimuli in Experiment 1. Each filled circle represents the RF of one macro-contact ($n_{contact}$=81). The radius of the circles represents the size of the RFs. C, Comparison of RF_LFA, RF_LGA, and RF_HGA sizes estimated in Experiment 1. D, Locations and sizes of RF_LFA, RF_LGA, and RF_HGA estimated with 3°×3° checkerboard stimuli in Experiment 2. E, Locations and sizes of RF_LFA, RF_LGA, and RF_HGA estimated with 1°×1° checkerboard stimuli in Experiment 2. F, Comparison of RF_LFA, RF_LGA, and RF_HGA sizes estimated in Experiment 2. G, Comparison of onset latencies among LFA, LGA, and HGA in Experiment 2. RMS, root mean square; error bars, standard error; *, $P<0.05$; **, $P<0.01$; ***, $P<0.001$; sig., significant; n.s., not significant.

Second, LFA may reflect the lateral connectivity from neighboring neurons (Angelucci et al., 2017; Gilbert et al., 1990; Stettler et al., 2002), which would lead to similar latencies among LFA, LGA, and HGA. To test these two explanations, we compared the onset latencies of visually evoked LFA, LGA, and HGA at each RF center in Experiment 2. A repeated-measures ANOVA of the LFP component showed no significant main effect on latencies (LFA: (89.6±8.3) ms; LGA: (71.0±4.7) ms; HGA: (94.8±8.1) ms; $F_{2,32}$=2.662, P=0.085), supporting the second explanation (Figure 2G).

RF estimated from spiking activity

RF is typically defined by spiking activity. It remains elusive how RF defined by spiking activity relates to RF defined by LFP. Thus, in Experiment 3, we took a rare opportunity to simultaneously record LFPs and spiking activity using microwires implanted in V1 of two subjects (Figure 3A; Figure S2 in Supporting Information).

We isolated 55 units from two RF mapping sessions for P469 and four RF mapping sessions for P659 (Table S2 and Figure S3

Figure 3. RF_{spike}, RF_{LFA}, RF_{LGA}, and RF_{HGA} mapping using microwires. A, Schematic description of the macro-micro electrode and the location of the microwires in P659. For P659, the 40 μm diameter microwires at the tip of the macro-micro electrode (black arrowhead) were localized in the ventral part of V1. B, RF_{spike} mapping procedure of an example recording (P659_Mi03_Session#1). A raster plot of spikes around stimulus onset (sorted by mapping positions, left) and the averaged PSTH waveforms at three example positions (corresponding trials in the raster plot are marked by numbers, right) are shown. Shaded areas indicate the standard errors of the waveforms. C, RMS map of spiking activity (upper) and two-dimensional Gaussian fit (lower) calculated for the example microwire shown in panel (B). The white ellipse indicates the RF_{spike} contour. RMS, root mean square. D, Comparison of RF_{spike}, RF_{LFA}, RF_{LGA}, and RF_{HGA} sizes ($n_{recording}$=14). Error bars, standard error; *, $P<0.05$.

in Supporting Information). We identified 46 visually responsive units by the presence of significant visually evoked spiking activity to at least one mapping position. In further analyses, we pooled the spiking activities of visually responsive units identified from the same microwire per session, resulting in a sample size of 29 (three single-unit recordings and two multi-unit recordings for P469, 11 single-unit recordings, and 13 multi-unit recordings for P659).

For the 29 microwires with visually responsive units, we further examined the significance of their visually evoked LFA, LGA, and HGA. For each mapping session, we defined a microwire recording with at least one visually responsive unit

and visually responsive LFA, LGA, and HGA as a visually responsive recording ($n_{recording}$=14, including six single-unit recordings and eight multi-unit recordings; Table S2 in Supporting Information).

For each of the 14 visually responsive recordings, we estimated RF sizes and locations from spiking activity (i.e., RF_{spike}), LFA, LGA, and HGA (see Figure 3B and C for an example recording). Note that RF_{spike} estimated for subject P469 had an average size of 0.5° at the eccentricity of about 4.3°, and RF_{spike} estimated for subject P659 had an average size of 0.6° at the eccentricity of about 6.2°. These results are in line with a recent attempt to estimate single-unit RFs using fMRI in human V1, which indicates that they are smaller than the estimated population RFs (Keliris et al., 2019). Further, previous studies have shown that the RF sizes of single-units in macaque V1 at similar eccentricities had a value of 0.1°–1.5° (Blasdel and Fitzpatrick, 1984; Gattass et al., 1981; Levitt and Lund, 2002). Therefore, the RF_{spike} sizes in human V1 are generally in agreement with those in macaque V1.

We found a significant difference among the sizes of RF_{spike} (0.5°±0.1°), RF_{LFA} (1.0°±0.1°), RF_{LGA} (0.5°±0.1°), and RF_{HGA} (0.6°±0.1°) ($F_{3,39}$=6.078, P=0.002; one-way repeated-measures ANOVA). Post hoc tests revealed that the sizes of RF_{LFA} were significantly larger than those of RF_{spike} (P=0.036; Figure 3D). The sizes of RF_{spike} were not significantly different from those of RF_{LGA} and RF_{HGA} (both $P>0.05$). To be noted, the sizes of RF_{LFA} were larger than those of RF_{LGA} and RF_{HGA} with marginal significance (RF_{LFA} vs. RF_{LGA}: P=0.060; RF_{LFA} vs. RF_{HGA}: P=0.085), consistent with the findings via macro-contacts in Experiments 1 and 2. For RF locations, no significant difference was found in either the eccentricity ($F_{3,39}$=0.347, P=0.791) or the polar angle ($F_{3,39}$=2.619, P=0.064; one-way repeated-measures ANOVAs).

We further quantified the spatial relationship between RF_{spike} and LFP RFs (RF_{LFA}, RF_{LGA}, and RF_{HGA}) using an overlap coefficient (OC) index (Winawer and Parvizi, 2016). For two RFs, an OC index of 1 indicates perfect overlap, and 0 indicates no overlap (Supplementary Methods for details). Results showed that the three LFP RFs significantly differed in their OC indices with RF_{spike} ($F_{2,26}$=10.438, P=4.701×10⁻⁴; repeated-measures ANOVA). Post hoc tests showed that, compared with RF_{LFA}, RF_{LGA} and RF_{HGA} exhibited higher OC indices with RF_{Spike} (RF_{LFA} vs. RF_{LGA}: P=0.033; RF_{LFA} vs. RF_{HGA}, P=0.003; Figure S4 in Supporting Information). No significant difference was found between RF_{LGA} and RF_{HGA} ($P>0.1$). These results suggest that RF_{Spike} can be better approximated by RF_{LGA} and RF_{HGA} than by RF_{LFA}.

Temporal relationships

The size similarity of RF_{LGA} and RF_{HGA} to RF_{spike} implies that they might have the same neuronal origin. One common evaluation of the neuronal origin of an LFP component is to calculate its temporal relationship with spiking activity (Mukamel et al., 2005; Ray et al., 2008a). In Experiment 3, we performed cross-correlation tests between the peri stimulus time histogram (PSTH) of spiking activity and the waveforms of LFA, LGA, and HGA evoked by the 1°×1° checkerboard presented around each RF_{spike} center for the 14 visually responsive recordings. We used the maximum cross-correlation coefficients to quantify the strength of LFP-spike correlations (i.e., LFA-spike, LGA-spike,

and HGA-spike correlations).

As shown by the examples in Figure 4A, some recordings exhibited the strongest correlation between spiking activity and HGA, while others showed the strongest correlation between spiking activity and LGA. Low LFA-spike correlations were observed consistently across recordings. Overall, we found a significant main effect of the LFP-spike correlation type ($F_{2,26}$=12.329, P=1.715×10^{-4}; one-way repeated-measures ANOVA). Specifically, the LFA-spike correlation (0.380±0.051) was significantly weaker than the LGA-spike (0.628±0.034) and HGA-spike (0.686±0.029) correlations (LFA $vs.$ LGA: P=0.023; LFA vs. HGA: P=0.004; post hoc tests). No significant difference was found between the HGA-spike correlation and the LGA-spike correlation (P=0.250; Figure 4B). These results revealed a close temporal relationship between LGA/HGA and spiking activity in human visual cortex.

We further characterized the temporal relationship by studying the LFPs around the occurrence of spikes. For the 29 microwires with visually responsive units, we extracted the spike-triggered average (STA) of the LFP (Figure 4C) and computed the normalized spike-triggered spectrum (nSTS; Figure 4D). nSTS measures LFP power locked to the spiking activity and is suitable for addressing the issue of spike-LFP coupling (Ray and Maunsell, 2011a). We found that the nSTS power significantly increased above zero at frequencies down to 24 Hz (P<0.05 with Bonferroni correction, t-test; Figure 4D), covering the frequency ranges of LGA and HGA. We submitted the nSTS powers averaged over LFA, LGA, and HGA frequency ranges to a one-way repeated-measures ANOVA, and found a significant main effect of the frequency range ($F_{2,56}$=28.770, P=2.542×10^{-9}). Post hoc tests revealed that the nSTS power in the LFA range was significantly lower than those in the LGA range (P=5.108×10^{-5}) and the HGA range (P=1.570 ×10^{-5}), while the nSTS power in the LGA range was significantly lower than that in the HGA range (P=1.636×10^{-4}; Figure 4E). These findings align with the correlation results, indicating a stronger spike-LFP coupling for LGA/HGA than LFA.

DISCUSSION

In this study, we estimated the sizes and locations of RF$_{LFA}$, RF$_{LGA}$, RF$_{HGA}$, and RF$_{spike,}$ combining macro-contact and microwire recordings in human visual cortex. We found that although the four RFs were nearly identical in location, they differed in size. Specifically, the sizes of RF$_{LFA}$ were remarkably larger than those of RF$_{LGA}$, RF$_{HGA}$, and RF$_{spike}$, while no difference was found among the sizes of RF$_{LGA}$, RF$_{HGA}$, and RF$_{spike}$. For the first time, we revealed that the RF$_{spike}$ sizes in human V1 were generally consistent with those in macaque V1. Furthermore, LGA and HGA, but not LFA, showed high correlations with spiking activity in temporal profile. These findings suggest that, in terms of RF estimation and temporal profile measurement, RF$_{LGA}$ and RF$_{HGA}$ are potential surrogates of RF$_{spike}$ if spiking activity cannot be obtained in human visual cortex.

We found that RF sizes estimated from LFA were significantly larger than those estimated from LGA, HGA, and spiking activity. Previous studies revealed that RFs in visual cortex have a center-surround organization (Bauer et al., 1995; Gieselmann and Thiele, 2008). That is, neurons respond to visual stimuli inside their RF and are also modulated by stimuli surrounding their RF

(Angelucci et al., 2017). Thus, a possible explanation for larger RF$_{LFA}$ sizes is that LFA is involved in surround modulation mechanisms, which integrate information inside and outside RF$_{spike}$ and probably reflect dendritic computations of excitatory and inhibitory inputs (Adesnik et al., 2012; Buzsáki and Draguhn, 2004). Researches on the center-surround organization of RFs and their spatial extent in human visual cortex rely primarily on fMRI methodologies (e.g., Fracasso et al., 2016; Williams et al., 2003). Recently, an innovative approach combining 7 T fMRI with pRF modeling has revealed that, at the eccentricity of 2°, the pRF surround size was approximately three times larger than the pRF center size (Fracasso et al., 2016). This ratio is close to the receptive field size ratio between the LFA and LGA/HGA in the present study. Notably, neurophysiological studies on non-human primates have suggested that the spatial extent of surround modulation originating from lateral connections is also typically two to three times larger than the diameter of the classical RF; in contrast, modulations from feedback connections are more spatially extensive (Angelucci et al., 2002). Combined with our findings that LFA, LGA, and HGA had similar onset latencies, the larger size of RF$_{LFA}$ likely results from lateral connections from neighboring neurons. Another possible explanation is that LFAs contain endogenous fluctuations that are not driven by visual stimulation $per se$. These fluctuations exhibit less tuning to stimulus attributes such as spatial location, resulting in larger RF$_{LFA}$ sizes. This explanation is supported by a previous study showing that low-frequency LFPs (<24 Hz) had strong noise correlations but weak signal correlations, indicating that they shared a common source of noises unrelated to the stimulus (Belitski et al., 2008).

Gamma-range activities (>30 Hz), which can be roughly divided into LGA and HGA, have been implicated in visual information processing (Brunet and Fries, 2019; Hermes et al., 2014; Hermes et al., 2015; Hermes et al., 2019; Lu et al., 2021; Peter et al., 2019; Zhang et al., 2020). There has been an ongoing debate on whether LGA and HGA in visual cortex are functionally distinct in encoding visual features. In monkey V1, LGA increased with stimulus size, but HGA decreased when the stimulus became larger (Dubey and Ray, 2020; Ray and Maunsell, 2011a). A recent study also revealed that LGA was prominently modulated by stimulus size and shape, while HGA was strongly modulated by location instead (Fischer and Wegener, 2021). In contrast, most intracranial recording studies in human visual cortex mainly investigated HGA (Davidesco et al., 2013; Golan et al., 2017; Martin et al., 2019; Zhou et al., 2019), leaving LGA largely unexplored. Until recently, Bartoli et al. (2019) found that LGA, but not HGA, was strongly tuned to contrast and hue, suggesting distinct functional roles of LGA and HGA in human visual cortex. In the current study, we found that the RFs estimated from LGA and HGA had similar sizes and locations in both macro-contact and microwire recordings. Given that LGA and HGA could be differentially modulated by stimulus size (Dubey and Ray, 2020; Ray and Maunsell, 2011a), one possible reason why we did not find the functional dissociation between LGA and HGA might be that we used relatively small and spatially discrete stimuli, whereas previous studies used larger and even full-screen visual stimuli (Bartoli et al., 2019; Hermes et al., 2015; Hermes et al., 2019; Winawer et al., 2013; Winawer and Parvizi, 2016). Delving deeper into the functional roles of gamma-range activities not only enhances our comprehension of the intricate mechanisms underlying visual proces-
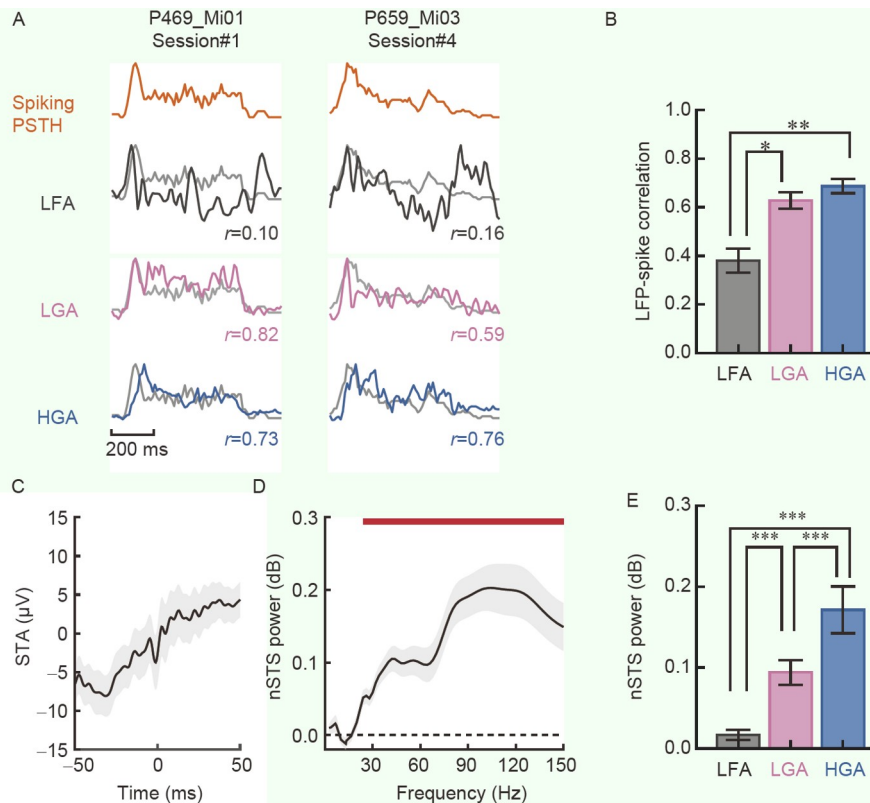
Figure 4. Temporal coupling between spiking activity and LFP components. A, Waveforms of spiking PSTH (orange), LFA (dark grey), LGA (pink), and HGA (blue) of two example microwires. The grey lines plotted with the LFP waveforms are the corresponding PSTH waveforms. The LFP-spike correlation coefficients (r) are also shown. B, Comparison of the LFP-spike correlation coefficients among different LFP components ($n_{recording}$=14). Compared with LFA, LGA and HGA showed stronger correlations with spiking activity in temporal profile. C, Mean STA of visually responsive units (n=29; shaded area: standard error). D, Mean nSTS as a function of frequency. The red line indicates frequencies at which nSTS showing values significantly above zero. E, Comparison of the nSTS power averaging across the frequency ranges of LFA, LGA, and HGA. Error bars, standard error; *, $P<0.05$; **, $P<0.01$; ***, $P<0.001$.

sing but also illuminates new prospects for developing innovative neuromodulation therapies targeting visual cortex (Beauchamp et al., 2020; Fu et al., 2021; Zhang et al., 2021).

Temporal correlation between gamma-range activities and spiking activity has been explored in animal models (Belitski et al., 2008; Burns et al., 2010; Rasch et al., 2008; Ray et al., 2008a; Ray et al., 2008b; Ray and Maunsell, 2011a; Ray and Maunsell, 2011b) and human subjects (Mukamel et al., 2005; Mukamel et al., 2011; Nir et al., 2007; Self et al., 2016). Studies using animal models demonstrated a robust coupling between HGA and spiking activity (Belitski et al., 2008; Burns et al., 2010; Ray et al., 2008a; Ray and Maunsell, 2011a), although recent evidence suggested that this coupling may be restricted to the HGA originated from the granular-infragranular layer (Leszczyński et al., 2020). Conversely, the relationship between LGA and spiking activity remains contentious, with some studies demonstrating strong coupling (Burns et al., 2010) and others reporting weak association (Ray et al., 2008a; Ray and Maunsell, 2011a). Furthermore, it has been discovered that the coupling between gamma-range activity and spiking activity is influenced by the spatial frequency of visual stimuli (Han et al., 2021). Using microwire recording in human auditory cortex, a series of studies revealed that the temporal profiles of gamma-range activities (40–130 Hz) were strongly correlated with spiking activity during both passive listening and resting state (Mukamel et al., 2005; Mukamel et al., 2011;

Nir et al., 2007). To date, the only microwire study of human visual cortex also found that gamma-range activities (40–140 Hz) and neuronal spiking could be co-modulated by orientation and contrast (Self et al., 2016). In line with these findings, we revealed that the temporal profiles of both LGA and HGA were strongly correlated with neuronal spiking activities (mean correlation coefficients>0.6) in human visual cortex. The strong HGA-spike correlation at the group level is also consistent with previous macaque studies (Kreiman et al., 2006; Ray et al., 2008a; Ray and Maunsell, 2011a). Meanwhile, the strong spike-LGA correlation could be explained by a recently discovered class of neurons with strong LGA synchronization in macaque V1 (Onorato et al., 2020). In their study, Onorato and colleagues showed that these LGA-synchronized neurons were characterized by a narrow spike waveform. In the future, it would be of great interest to probe whether LGA and HGA in human visual cortex originate from different neuronal populations.

In sum, using direct electrophysiological recordings in human visual cortex, we explored the relationships between spiking activity and different LFP components (LFA, LGA, and HGA) in RF estimation and temporal profile measurement. We revealed that LGA and HGA, but not LFA, can closely approximate neuronal spiking activity in these two respects. Moreover, to the best of our knowledge, the current study is the first quantitative report of neuronal RF properties in human V1.

MATERIALS AND METHODS

Human subjects

All human subjects were patients with drug-resistant epilepsy who underwent invasive stereo-electroencephalogram monitoring for potential surgical treatments at the Sanbo Brain Hospital of Capital Medical University (Beijing, China). LFPs were recorded from 22 subjects (17 males, mean age 27.3 years old) via macro-contacts (Experiments 1 and 2). Simultaneous recording of LFPs and spiking activity was performed with two subjects (P469: female, 32 years old; P659 male, 25 years old) via microwires (Experiment 3). Demographic information and implantation details are listed in Table S1 in Supporting Information. All subjects provided written, informed consent to participate in the experiments. All experimental procedures were approved by the Ethics Committee of the Sanbo Brain Hospital of Capital Medical University and the Human Subject Review Committee of Peking University.

Stereo-electrodes

Twenty patients were implanted with stereo-electrodes. Each stereo-electrode had 8–16 macro-contacts (0.8 mm in diameter, 2 mm in length, spacing 3.5 mm apart; Huake Hengsheng Medical Technology Co. Ltd., Beijing, China) (Figure S1A in Supporting Information). All stereo-electrode implantations were determined based on clinical reasons.

Macro-micro electrodes

Two patients (P469 and P659) were implanted with macro-micro electrodes (BF08R-SP05X-000, WB09R-SP00X-014, Ad-Tech Medical Instrument Corp., USA) in their visual cortex. Each macro-micro electrode had eight macro-contacts (1.3 mm in diameter, 1.57 mm in length, spacing 5 mm apart) and nine microwires at the tip (Figure S1B in Supporting Information). All macro-micro electrode implantations were determined based on clinical reasons.

Electrode localization and selection

For electrode localization, we first co-registered the post-implant CT images to the pre-implant T1-weighted MRI scans for each subject using the SPM12 toolbox (available at https://www.fil.ion.ucl.ac.uk/spm/software/spm12/) (Friston et al., 2011). Then, we identified individual electrodes on the aligned CT images and calculated the coordinates of macro-contacts using the Brainstorm toolbox (available at http://neuroimage.usc.edu/brainstorm) (Tadel et al., 2011). Since microwires were usually invisible on the post-implant CT images, their coordinates were estimated by combining the nearest macro-contact coordinates and the macro-micro electrode geometry (Bartoli et al., 2019; Self et al., 2016).

Only one subject (P469) participated in an fMRI retinotopic mapping experiment before electrode implantation. For P469, we defined her retinotopic visual areas (V1, V2, and V3) using a standard phase-encoded method (Engel et al., 1997; Sereno et al., 1995) (for details, see Supplementary Methods, Figure S2A and B in Supporting Information).

For the other 21 subjects, we selected macro-contacts localized in V1, V2, and V3 based on the anatomical identification in individual brains. We first performed cortical segmentation and reconstruction using individual pre-implant T1-weighted MRI scans in Freesurfer (version 6.0) (Dale et al., 1999). We then mapped V1, V2, and V3 onto individual cortical surfaces using a publicly available anatomical atlas (Benson et al., 2014) with codes from the Neuropythy toolbox (available at https://github.com/noahbenson/neuropythy/). We projected each macro-contact to the nearest vertex on the individual cortical surface using MATLAB (v2017b) function "dnsearch". Macro-contacts were then assigned to V1, V2, and V3 based on the projected vertices. The "dnsearch" function also yielded the distance to the cortical surface for each macro-contact. Since the gray matter in human visual cortex is about 2–3 mm thick (Fischl and Dale, 2000) and macro-contacts had a maximum length of 2 mm, macro-contacts farther than 5 mm from the cortical surface were considered localized in white matter, and excluded from further analyses. Macro-contacts localized outside V1, V2, and V3 were also excluded from further analyses. For each macro-micro electrode, the anatomical identifications of microwires were referred to that of the nearest macro-contact.

To visualize all macro-contacts localized to visual cortex in a common space, we transformed the macro-contact coordinates into MNI coordinates and displayed them on a flattened cortical template (cvs_avg35_inMNI152) (Figure 1C). We also visualized the stereo-electrodes and macro-micro electrodes in individual brains (see Figure S1 in Supporting Information for locations of macro-contacts; see Figure 3A and Figure S2C in Supporting Information for locations of microwires).

Experimental procedure

All experiments were conducted in quiet and dimly lighted patient rooms. Subjects were seated in bed during the experiments, with their head stabilized using a chin rest. Visual stimuli were generated and controlled using MATLAB and Psychtoolbox-3 extensions (Kleiner et al., 2007). They were presented on a laptop (14-inch, Thinkpad T590) or an LCD monitor (23.8-inch, Dell SE2416H) at a viewing distance of 40–60 cm.

Experiment 1: RF mapping using macro-contacts and 3°×3° checkerboard stimuli

All 22 subjects participated in Experiment 1 (Table S1 in Supporting Information). We adopted an RF mapping procedure from a previous ECoG study (Yoshor et al., 2007). In each mapping run, a black-and-white checkerboard stimulus subtending 3°×3° of visual angle (checker size: 0.33°×0.33°, mean luminance: 32.0 cd m^{-2}) was flashed at different mapping positions on the monitor to fill either an 11×9 (full visual field) or a 6×9 (half visual field contralateral to the implanted macro-contacts) grid (Figure 1A). The luminance of the grey background was 11.3 cd m^{-2}. Eight subjects received RF mapping of the full visual field, and 14 received RF mapping of the contralateral visual field. Each subject completed 15–20 mapping runs, resulting in 15–20 trials for each mapping position (one trial per mapping position per run). Checkerboard stimuli were presented for 500 ms at a temporal rate of 1 Hz. Subjects were asked to perform a fixation task by responding to color changes of the fixation point with mouse clicking (press the left button when changing to red and press the right button when changing to green). We tracked eye positions using an Eyelink

Portable Duo tracker (SR Research, Canada) in 17 subjects (Table S1 in Supporting Information) and aborted trials in which the eye positions deviated away from the fixation point more than 1.0°. 13.9% of the total trials were excluded from further analyses.

Experiment 2: RF mapping using macro-contacts and 1°×1° checkerboard stimuli

Five subjects participated in Experiment 2 (Table S1 in Supporting Information), which was similar to Experiment 1. For each run, a black-and-white checkerboard stimulus subtending 1°×1° of visual angle (checker size: 0.33°×0.33°, mean luminance: 32.0 cd m^{-2}) was flashed at different positions on the monitor within an adjusted visual field optimized based on the results of Experiment 1. The luminance of the grey background was the same as in Experiment 1. Each subject completed 15–20 mapping runs (one trial per mapping position per run). We tracked eye positions for all subjects. Trials in which the eye positions deviated away from the fixation point more than 1.0° were aborted (6.9% of the total trials).

Experiment 3: RF mapping using microwires and 1°×1° checkerboard stimuli

Two subjects (P469 and P659) participated in Experiment 3 (Table S1 in Supporting Information). The mapping procedure was identical to that in Experiment 2. To obtain sufficient single-unit and multi-unit signals, subjects completed multiple sessions (2 sessions for Subject P469, 4 sessions for Subject P659; Table S2 in Supporting Information). Each session consisted of 10–15 mapping runs (one trial per mapping position per run). Eye positions were monitored, and only 0.4% of the total trials were excluded using the same criteria in Experiments 1 and 2.

Electrophysiological recording via macro-contacts

Macro-contact signals were recorded at a sampling rate of 512 Hz using a Nicolet video-EEG monitoring system (Thermo Nicolet Corp., USA) without any online filtering. Both the reference and ground electrodes were placed on the forehead of subjects. Macro-contact impedances were kept below 50 kΩ throughout the recording. All further processing was performed offline.

Electrophysiological recording via microwires

Microwire signals were recorded at a sampling rate of 32 kHz using an ATLAS neurophysiology system (Neuralynx Inc., USA). According to a previous study, the pre-implantation *ex-vivo* impedances of the microwires were 50–500 kΩ, and the post-implantation *in vivo* impedances were typically 20–30 kΩ higher than the pre-implantation values (Misra et al., 2014). Signals were amplified using an HS-10-CHET pre-amplifier. For each macro-micro electrode, one microwire served as the local reference. We online monitored spiking activity using the Pegasus software (Neuralynx Inc.). Unfiltered raw signals were stored for offline extraction of both LFPs and spiking activity.

Preprocessing of macro-contact signals

All signal processing and statistical tests were performed using publicly available toolboxes and custom scripts in Matlab. In Experiments 1 and 2, we imported raw macro-contact signals into the EEGLAB toolbox (version 14.1.1b) (Delorme and Makeig, 2004) for visual inspection. Macro-contacts that contained epileptic activities or artifacts were excluded from further analyses. Signals were notch-filtered (50 Hz and harmonics) and then band-pass filtered (0.5–200 Hz) to generate broadband LFPs. Next, we filtered the broadband LFPs to obtain three LFP components: low-frequency activity (LFA, 0.5–30 Hz), low-gamma activity (LGA, 30–60 Hz), and high-gamma activity (HGA, 60–150 Hz). Two-way least-squares finite impulse response (FIR) filters were used ("eegfilt" function from the EEGLAB toolbox). We then extracted the amplitude envelope of each LFP component using the Hilbert transform. Finally, broadband LFPs and amplitude envelopes of the three LFP components were segmented around stimulus onset (−100–800 ms) and corrected against the baseline (−100–0 ms).

Preprocessing of microwire signals

LFPs

Raw microwire signals in Experiment 3 were down-sampled to 2,000 Hz for LFP extraction. We then obtained LFA, LGA, and HGA using the pipeline described above for processing macro-contact signals.

Spiking activity

In Experiment 3, we obtained spiking activity using the Osort toolbox (Rutishauser et al., 2006). We filtered the raw microwire signals with a zero-phase lag band-pass filter (300–3,000 Hz; Figure S3A in Supporting Information). Spikes were detected and sorted using an automatic algorithm (Figure S3B and C in Supporting Information). We measured the quality of the isolated units using the following criteria: (i) the percentage of inter-spike intervals smaller than 3 ms (0.57%±0.09%); (ii) the mean firing rate during each recording session ((1.27±0.18) Hz); (iii) the signal-to-noise ratio (SNR) of the spike waveform (3.64±0.15); (iv) the modified coefficient of variation (CV2) (1.05±0.01); (v) the pairwise distance between all pairs of isolated units on the same microwires (11.60±0.61; Figure S3D–H in Supporting Information) (Aquino et al., 2020; Minxha et al., 2020). Overall, we isolated 55 units from 6 recording sessions (7 units from subject P469 and 48 units from subject P659; Table S2 in Supporting Information).

For each unit, we segmented the spike trains into epochs from −100 to 800 ms around stimulus onset. PSTHs were constructed using non-overlapping 10 ms bins and then smoothed using a 50 ms square window with 10 ms steps.

Identification of visually responsive macro-contacts and units

In Experiments 1 and 2, we defined visually responsive macro-contacts by the presence of a significant visually evoked broadband LFP to at least one mapping position. For a mapping position, the significance of a visually evoked broadband LFP was defined by two criteria: (i) the amplitude in the early response window (0–200 ms) exhibited at least one significant cluster longer than 10 ms (Wilcoxon rank-sum tests, $P<0.05$; false discovery rate correction); (ii) the standard deviation of the amplitude in the early response window was three times larger than the standard deviation of the baseline. For each visually responsive macro-contact, we tested the significance of LFA,

LGA, and HGA using the same criteria described above.

In Experiment 3, we defined visually responsive units by the presence of significant visually driven spiking activity to at least one mapping position. For a mapping position, significant visually driven spiking activity was defined by two criteria: (i) the averaged firing rate at this mapping position was three standard deviations above the averaged firing rate at all mapping positions; (ii) the standard deviation of firing rate in the early response window (0–200 ms) were three times larger than the standard deviation of the baseline.

We also tested the significance of LFA, LGA, and HGA for microwires with at least one visually responsive unit using the same criteria described above for macro-contact signals. For each mapping session, we defined the recording from a microwire with both significant spiking activity and significant LFP components as a visually responsive recording.

Estimation of the location and size of RFs

For each macro-contact or microwire recording, we estimated the size and location of the RF_{LFA}, RF_{LGA}, RF_{HGA}, and RF_{spike} using the same pipeline. We calculated the root mean square (RMS) of the visually evoked response (LFA, LGA, HGA, or spiking activity) from 0 to 800 ms after stimulus onset at each mapping position. To reduce noise, we substituted the RMS value in mapping positions without significant neuronal responses with the averaged RMS value of all mapping positions. We fitted a 2D Gaussian function to the RMS values for all mapping positions (Self et al., 2016; Yoshor et al., 2007). The RF location was defined as the coordinates of the fitted Gaussian function center. The RF size was determined by averaging the FWHM of the two axes from the fitted Gaussian function.

Evaluation of onset latency

In Experiment 2, we measured the onset latency of visually evoked LFA, LGA, and HGA using an established method (Bartoli et al., 2019; Foster et al., 2015). The response waveforms evoked by the checkerboard nearest the RF location were selected. We first smoothed single-trial responses with a 100 ms Gaussian sliding window. We then defined the response threshold as the 75th percentile of the response amplitude across all trials for each macro-contact. For each trial, we marked the first time point at which the response amplitude exceeded the response threshold (lasted for at least 40 ms in the time window between −100 to 500 ms) and defined a 300 ms window of interest around the time point (100 ms before and 200 ms after). Next, we segmented the window into 50 ms bins with 90% overlap and fitted each bin using linear regression. The first time point of the bin with the largest slope and lowest residual error was then defined as the onset of the trial. The onset latency of a macro-contact was defined as the averaged latency across trials.

Evaluation of temporal relationships

In Experiment 3, we used cross-correlation tests to examine the temporal correlations between spiking activity and LFP components (LFA, LGA, and HGA) for all visually responsive recordings (n=14). For each visually responsive microwire, we selected the PSTH of spiking activity and waveforms of the three LFP components evoked by the 1°×1° checkerboard presented

around each RF_{spike} center. We then downsampled LFA, LGA, and HGA waveforms to match the 100 Hz sampling rate of the PSTH. Next, we calculated cross-correlation coefficients between the PSTH and the waveforms of LFA, LGA, and HGA with time lags between −100 to 100 ms. Finally, the maximal correlation coefficients were Fisher-z transformed for statistical analyses.

We further extracted the STA of the LFP for visually responsive units (n=29) using codes and pipelines from the Fieldtrip toolbox (Oostenveld et al., 2011). In short, spike-locked artifacts were removed by replacing the ±2 ms portion of the LFP around the occurrence of the spikes recorded from the same microwire with NaNs. Next, the spike-triggered spectrum (STS) was computed using the "mtmconvol" method. The STS contains a spike-locking component and a spike-unlocking component with a 1/f power spectrum, and only the first component is of interest here. The spike-unlocking component can be estimated by computing the STS after randomizing the timing of spikes (i.e., randomized STS, or "rSTS"). Therefore, we extracted the spike-locking component (i.e., normalized STS, or "nSTS") by taking the difference between log(STS) and log(rSTS) (Ray and Maunsell, 2011a). Finally, nSTS values were averaged over the LFA, LGA, and HGA frequency ranges for statistical comparisons.

Statistical analyses

We performed statistical analyses using custom scripts in Matlab. To identify visually responsive LFPs, we used Wilcoxon rank-sum tests with false discovery rate (FDR) corrections for multiple comparisons. Moreover, we used repeated-measures ANOVAs to compare RF sizes, locations, latencies, and LFP-spike correlation coefficients. For post hoc tests, we reported Bonferroni corrected P-values. The alpha level was set at 0.05.

References

Adesnik, H., Bruns, W., Taniguchi, H., Huang, Z.J., and Scanziani, M. (2012). A neural circuit for spatial summation in visual cortex. Nature 490, 226–231.

Andoni, S., Tan, A., and Priebe, N. (2013). The cortical assembly of visual receptive fields. In: Werner, J.S., and Leo, M., eds. The New Visual Neurosciences. Cambridge: MIT Press. 367–380.

Angelucci, A., Levitt, J.B., Walton, E.J.S., Hupé, J.M., Bullier, J., and Lund, J.S. (2002). Circuits for local and global signal integration in primary visual cortex. J Neurosci 22, 8633–8646.

Angelucci, A., Bijanzadeh, M., Nurminen, L., Federer, F., Merlin, S., and Bressloff, P.C. (2017). Circuits and mechanisms for surround modulation in visual cortex. Annu Rev Neurosci 40, 425–451.

Aquino, T.G., Minxha, J., Dunne, S., Ross, I.B., Mamelak, A.N., Rutishauser, U., and O'Doherty, J.P. (2020). Value-related neuronal responses in the human amygdala during observational learning. J Neurosci 40, 4761–4772.

Bartoli, E., Bosking, W., Chen, Y., Li, Y., Sheth, S.A., Beauchamp, M.S., Yoshor, D., and Foster, B.L. (2019). Functionally distinct gamma range activity revealed by stimulus tuning in human visual cortex. Curr Biol 29, 3345–3358.e7.

Bastos, A.M., Vezoli, J., Bosman, C.A., Schoffelen, J.M., Oostenveld, R., Dowdall, J.R.,

De Weerd, P., Kennedy, H., and Fries, P. (2015). Visual areas exert feedforward and feedback influences through distinct frequency channels. Neuron 85, 390–401.

Bauer, R., Brosch, M., and Eckhorn, R. (1995). Different rules of spatial summation from beyond the receptive field for spike rates and oscillation amplitudes in cat visual cortex. Brain Res 669, 291–297.

Beaulieu-Laroche, L., Toloza, E.H.S., van der Goes, M.S., Lafourcade, M., Barnagian, D., Williams, Z.M., Eskandar, E.N., Frosch, M.P., Cash, S.S., and Harnett, M.T. (2018). Enhanced dendritic compartmentalization in human cortical neurons. Cell 175, 643–651.e14.

Belitski, A., Gretton, A., Magri, C., Murayama, Y., Montemurro, M.A., Logothetis, N. K., and Panzeri, S. (2008). Low-frequency local field potentials and spikes in primary visual cortex convey independent visual information. J Neurosci 28, 5696–5709.

Benson, N.C., Butt, O.H., Brainard, D.H., and Aguirre, G.K. (2014). Correction of distortion in flattened representations of the cortical surface allows prediction of V1-V3 functional organization from anatomy. PLoS Comput Biol 10, e1003538.

Beauchamp, M.S., Oswalt, D., Sun, P., Foster, B.L., Magnotti, J.F., Niketeghad, S., Pouratian, N., Bosking, W.H., and Yoshor, D. (2020). Dynamic stimulation of visual cortex produces form vision in sighted and blind humans. Cell 181, 774–783.e5.

Blasdel, G.G., and Fitzpatrick, D. (1984). Physiological organization of layer 4 in macaque striate cortex. J Neurosci 4, 880–895.

Boldog, E., Bakken, T.E., Hodge, R.D., Novotny, M., Aevermann, B.D., Baka, J., Bordé, S., Close, J.L., Diez-Fuertes, F., Ding, S.L., et al. (2018). Transcriptomic and morphophysiological evidence for a specialized human cortical GABAergic cell type. Nat Neurosci 21, 1185–1195.

Bosking, W.H., Sun, P., Ozker, M., Pei, X., Foster, B.L., Beauchamp, M.S., and Yoshor, D. (2017). Saturation in phosphene size with increasing current levels delivered to human visual cortex. J Neurosci 37, 7188–7197.

Brunet, N.M., and Fries, P. (2019). Human visual cortical gamma reflects natural image structure. NeuroImage 200, 635–643.

Burns, S.P., Xing, D., and Shapley, R.M. (2010). Comparisons of the dynamics of local field potential and multiunit activity signals in macaque visual cortex. J Neurosci 30, 13739–13749.

Buzsáki, G., and Draguhn, A. (2004). Neuronal oscillations in cortical networks. Science 304, 1926–1929.

Dale, A.M., Fischl, B., and Sereno, M.I. (1999). Cortical surface-based analysis: I. Segmentation and surface reconstruction. NeuroImage 9, 179–194.

Davidesco, I., Harel, M., Ramot, M., Kramer, U., Kipervasser, S., Andelman, F., Neufeld, M.Y., Goelman, G., Fried, I., and Malach, R. (2013). Spatial and object-based attention modulates broadband high-frequency responses across the human visual cortical hierarchy. J Neurosci 33, 1228–1240.

Delorme, A., and Makeig, S. (2004). EEGLAB: an open source toolbox for analysis of single-trial EEG dynamics including independent component analysis. J Neurosci Methods 134, 9–21.

Dubey, A., and Ray, S. (2020). Comparison of tuning properties of gamma and high-gamma power in local field potential (LFP) versus electrocorticogram (ECoG) in visual cortex. Sci Rep 10, 5422.

Dumoulin, S.O., and Wandell, B.A. (2008). Population receptive field estimates in human visual cortex. NeuroImage 39, 647–660.

Engel, S.A., Glover, G.H., and Wandell, B.A. (1997). Retinotopic organization in human visual cortex and the spatial precision of functional MRI. Cereb Cortex 7, 181–192.

Fischer, B., and Wegener, D. (2021). Monkey V1 epidural field potentials provide detailed information about stimulus location, size, shape, and color. Commun Biol 4, 1–3.

Fischl, B., and Dale, A.M. (2000). Measuring the thickness of the human cerebral cortex from magnetic resonance images. Proc Natl Acad Sci USA 97, 11050–11055.

Foster, B.L., Rangarajan, V., Shirer, W.R., and Parvizi, J. (2015). Intrinsic and task-dependent coupling of neuronal population activity in human parietal cortex. Neuron 86, 578–590.

Fracasso, A., Petridou, N., and Dumoulin, S.O. (2016). Systematic variation of population receptive field properties across cortical depth in human visual cortex. NeuroImage 139, 427–438.

Friston, K.J., Ashburner, J.T., Kiebel, S.J., Nichols, T.E., and Penny, W.D. (2011). Statistical Parametric Mapping: The Analysis of Functional Brain Images. Amsterdam: Elsevier.

Fu, Y., Yan, W., Shen, M., and Chen, H. (2021). Does consciousness overflow cognitive access? Novel insights from the new phenomenon of attribute amnesia. Sci China Life Sci 64, 847–860.

Gattass, R., Gross, C.G., and Sandell, J.H. (1981). Visual topography of V2 in the macaque. J Comp Neurol 201, 519–539.

Gieselmann, M.A., and Thiele, A. (2008). Comparison of spatial integration and surround suppression characteristics in spiking activity and the local field potential in macaque V1. Eur J Neurosci 28, 447–459.

Gilbert, C.D., Hirsch, J.A., and Wiesel, T.N. (1990). Lateral interactions in visual cortex. Cold Spring Harb Symp Quant Biol 55, 663–677.

Golan, T., Davidesco, I., Meshulam, M., Groppe, D.M., Mégevand, P., Yeagle, E.M., Goldfinger, M.S., Harel, M., Melloni, L., Schroeder, C.E., et al. (2017). Increasing suppression of saccade-related transients along the human visual hierarchy. eLife 6, e27819.

Han, C., Wang, T., Yang, Y., Wu, Y., Li, Y., Dai, W., Zhang, Y., Wang, B., Yang, G., Cao, Z., et al. (2021). Multiple gamma rhythms carry distinct spatial frequency information in primary visual cortex. PLoS Biol 19, e3001466.

Hermes, D., Miller, K.J., Wandell, B.A., and Winawer, J. (2014). Stimulus dependence of gamma oscillations in human visual cortex. Cereb Cortex 25, 2951–2959.

Hermes, D., Miller, K.J., Wandell, B.A., and Winawer, J. (2015). Gamma oscillations in visual cortex: the stimulus matters. Trends Cogn Sci 19, 57–58.

Hermes, D., Petridou, N., Kay, K.N., and Winawer, J. (2019). An image-computable model for the stimulus selectivity of gamma oscillations. eLife 8, e47035.

Hubel, D.H., and Wiesel, T.N. (1959). Receptive fields of single neurones in the cat's striate cortex. J Physiol 148, 574–591.

Jensen, O., Bonnefond, M., Marshall, T.R., and Tiesinga, P. (2015). Oscillatory mechanisms of feedforward and feedback visual processing. Trends Neurosci 38, 192–194.

Kaas, J.H., and Herculano-Houzel, S. (2017). What makes the human brain special: key features of brain and neocortex. In: Opris, I., and Casanova, M.F., eds. The Physics of the Mind and Brain Disorders. Springer Series in Cognitive and Neural Systems. Cham: Springer. 3–22.

Keliris, G.A., Li, Q., Papanikolaou, A., Logothetis, N.K., and Smirnakis, S.M. (2019). Estimating average single-neuron visual receptive field sizes by fMRI. Proc Natl Acad Sci USA 116, 6425–6434.

Kleiner, M., Brainard, D., and Pelli, D. (2007). What's new in Psychtoolbox-3? Perception 36, 1–16.

Klink, P.C., Chen, X., Vanduffel, W., and Roelfsema, P.R. (2021). Population receptive fields in nonhuman primates from whole-brain fMRI and large-scale neurophysiology in virtual visual cortex. eLife 10, e67304.

Kreiman, G., Hung, C.P., Kraskov, A., Quiroga, R.Q., Poggio, T., and DiCarlo, J.J. (2006). Object selectivity of local field potentials and spikes in the macaque inferior temporal cortex. Neuron 49, 433–445.

Leszczyński, M., Barczak, A., Kajikawa, Y., Ulbert, I., Falchier, A.Y., Tal, I., Haegens, S., Melloni, L., Knight, R.T., and Schroeder, C.E. (2020). Dissociation of broadband high-frequency activity and neuronal firing in the neocortex. Sci Adv 6, eabb0977.

Levitt, J.B., and Lund, J.S. (2002). The spatial extent over which neurons in macaque striate cortex pool visual signals. Vis Neurosci 19, 439–452.

Lu, J., Luo, L., Wang, Q., Fang, F., and Chen, N. (2021). Cue-triggered activity replay in human early visual cortex. Sci China Life Sci 64, 144–151.

Mamelak, A.N. (2014). Ethical and practical considerations for human microelectrode recording studies. In: Fried, I., Rutishauser, U., Cerf, M., and Kreiman, G., eds. Single Neuron Studies of the Human Brain: Probing Cognition. Cambridge: MIT Press. 27–42.

Marg, E., Adams, J.E., and Rutkin, B. (1968). Receptive fields of cells in the human visual cortex. Experientia 24, 348–350.

Martin, A.B., Yang, X., Saalmann, Y.B., Wang, L., Shestyuk, A., Lin, J.J., Parvizi, J., Knight, R.T., and Kastner, S. (2019). Temporal dynamics and response modulation across the human visual system in a spatial attention task: an ECoG study. J Neurosci 39, 333–352.

Michalareas, G., Vezoli, J., van Pelt, S., Schoffelen, J.M., Kennedy, H., and Fries, P. (2016). Alpha-beta and gamma rhythms subserve feedback and feedforward influences among human visual cortical areas. Neuron 89, 384–397.

Misra, A., Burke, J.F., Ramayya, A.G., Jacobs, J., Sperling, M.R., Moxon, K.A., Kahana, M.J., Evans, J.J., and Sharan, A.D. (2014). Methods for implantation of micro-wire bundles and optimization of single/multi-unit recordings from human mesial temporal lobe. J Neural Eng 11, 026013.

Minxha, J., Adolphs, R., Fusi, S., Mamelak, A.N., and Rutishauser, U. (2020). Flexible recruitment of memory-based choice representations by the human medial frontal cortex. Science 368, eaba3313.

Mukamel, R., Gelbard, H., Arieli, A., Hasson, U., Fried, I., and Malach, R. (2005). Coupling between neuronal firing, field potentials, and fMRI in human auditory cortex. Science 309, 951–954.

Mukamel, R., Nir, Y., Harel, M., Arieli, A., Malach, R., and Fried, I. (2011). Invariance of firing rate and field potential dynamics to stimulus modulation rate in human auditory cortex. Hum Brain Mapp 32, 1181–1193.

Nir, Y., Fisch, L., Mukamel, R., Gelbard-Sagiv, H., Arieli, A., Fried, I., and Malach, R. (2007). Coupling between neuronal firing rate, gamma LFP, and BOLD fMRI is related to interneuronal correlations. Curr Biol 17, 1275–1285.

Onorato, I., Neuenschwander, S., Hoy, J., Lima, B., Rocha, K.S., Broggini, A.C., Uran,

C., Spyropoulos, G., Klon-Lipok, J., Womelsdorf, T., et al. (2020). A distinct class of bursting neurons with strong gamma synchronization and stimulus selectivity in monkey V1. Neuron 105, 180–197.e5.

Oostenveld, R., Fries, P., Maris, E., and Schoffelen, J.M. (2011). FieldTrip: open source software for advanced analysis of MEG, EEG, and invasive electrophysiological data. Comput Intell Neurosci 2011, 1–9.

Parvizi, J., and Kastner, S. (2018). Promises and limitations of human intracranial electroencephalography. Nat Neurosci 21, 474–483.

Perge, J.A., Zhang, S., Malik, W.Q., Homer, M.L., Cash, S., Friehs, G., Eskandar, E.N., Donoghue, J.P., and Hochberg, L.R. (2014). Reliability of directional information in unsorted spikes and local field potentials recorded in human motor cortex. J Neural Eng 11, 046007.

Peter, A., Uran, C., Klon-Lipok, J., Roese, R., van Stijn, S., Barnes, W., Dowdall, J.R., Singer, W., Fries, P., and Vinck, M. (2019). Surface color and predictability determine contextual modulation of V1 firing and gamma oscillations. eLife 8, e42101.

Pryluk, R., Kfir, Y., Gelbard-Sagiv, H., Fried, I., and Paz, R. (2019). A tradeoff in the neural code across regions and species. Cell 176, 597–609.e18.

Rasch, M.J., Gretton, A., Murayama, Y., Maass, W., and Logothetis, N.K. (2008). Inferring spike trains from local field potentials. J Neurophysiol 99, 1461–1476.

Ray, S., Crone, N.E., Niebur, E., Franaszczuk, P.J., and Hsiao, S.S. (2008a). Neural correlates of high-gamma oscillations (60–200 Hz) in Macaque local field potentials and their potential implications in electrocorticography. J Neurosci 28, 11526–11536.

Ray, S., Hsiao, S.S., Crone, N.E., Franaszczuk, P.J., and Niebur, E. (2008b). Effect of stimulus intensity on the spike-local field potential relationship in the secondary somatosensory cortex. J Neurosci 28, 7334–7343.

Ray, S., and Maunsell, J.H.R. (2011a). Different origins of gamma rhythm and high-gamma activity in macaque visual cortex. PLoS Biol 9, e1000610.

Ray, S., and Maunsell, J.H.R. (2011b). Network rhythms influence the relationship between spike-triggered local field potential and functional connectivity. J Neurosci 31, 12674–12682.

Rutishauser, U., Schuman, E.M., and Mamelak, A.N. (2006). Online detection and sorting of extracellularly recorded action potentials in human medial temporal lobe recordings, in vivo. J Neurosci Methods 154, 204–224.

Self, M.W., Peters, J.C., Possel, J.K., Reithler, J., Goebel, R., Ris, P., Jeurissen, D., Reddy, L., Claus, S., Baayen, J.C., et al. (2016). The effects of context and attention on spiking activity in human early visual cortex. PLoS Biol 14, e1002420.

Sereno, M.I., Dale, A.M., Reppas, J.B., Kwong, K.K., Belliveau, J.W., Brady, T.J., Rosen, B.R., and Tootell, R.B.H. (1995). Borders of multiple visual areas in humans revealed by functional magnetic resonance imaging. Science 268, 889–893.

Stettler, D.D., Das, A., Bennett, J., and Gilbert, C.D. (2002). Lateral connectivity and contextual interactions in macaque primary visual cortex. Neuron 36, 739–750.

Tadel, F., Baillet, S., Mosher, J.C., Pantazis, D., and Leahy, R.M. (2011). Brainstorm: a user-friendly application for MEG/EEG analysis. Comput Intell Neurosci 2011, 879716.

van Kerkoerle, T., Self, M.W., Dagnino, B., Gariel-Mathis, M.A., Poort, J., van der Togt, C., and Roelfsema, P.R. (2014). Alpha and gamma oscillations characterize feedback and feedforward processing in monkey visual cortex. Proc Natl Acad Sci USA 111, 14332–14341.

Wandell, B.A., Dumoulin, S.O., and Brewer, A.A. (2007). Visual field maps in human cortex. Neuron 56, 366–383.

Wandell, B.A., and Winawer, J. (2015). Computational neuroimaging and population receptive fields. Trends Cogn Sci 19, 349–357.

Werner, J.S., and Spillmann, L. (1990). Visual Perception: The Neurophysiological Foundations. New York: Academic Press.

Williams, A.L., Singh, K.D., and Smith, A.T. (2003). Surround modulation measured with functional MRI in the human visual cortex. J Neurophysiol 89, 525–533.

Wilson, C.L., Babb, T.L., Halgren, E., and Crandall, P.H. (1983). Visual receptive fields and response properties of neurons in human temporal lobe and visual pathways. Brain 106, 473–502.

Winawer, J., Kay, K.N., Foster, B.L., Rauschecker, A.M., Parvizi, J., and Wandell, B.A. (2013). Asynchronous broadband signals are the principal source of the BOLD response in human visual cortex. Curr Biol 23, 1145–1153.

Winawer, J., and Parvizi, J. (2016). Linking electrical stimulation of human primary visual cortex, size of affected cortical area, neuronal responses, and subjective experience. Neuron 92, 1213–1219.

Yoshor, D., Bosking, W.H., Ghose, G.M., and Maunsell, J.H.R. (2007). Receptive fields in human visual cortex mapped with surface electrodes. Cereb Cortex 17, 2293–2302.

Zanos, S., Zanos, T.P., Marmarelis, V.Z., Ojemann, G.A., and Fetz, E.E. (2012). Relationships between spike-free local field potentials and spike timing in human temporal cortex. J Neurophysiol 107, 1808–1821.

Zhang, Y., Zhang, Y.Y., and Fang, F. (2020). Neural mechanisms of feature binding. Sci China Life Sci 63, 926–928.

Zhang, Z., Zhang, H., Xie, C.M., Zhang, M., Shi, Y., Song, R., Lu, X., Zhang, H., Li, K., Wang, B., et al. (2021). Task-related functional magnetic resonance imaging-based neuronavigation for the treatment of depression by individualized repetitive transcranial magnetic stimulation of the visual cortex. Sci China Life Sci 64, 96–106.

Zhou, J., Benson, N.C., Kay, K., and Winawer, J. (2019). Predicting neuronal dynamics with a delayed gain control model. PLoS Comput Biol 15, e1007484.